Supplement of The Cryosphere, 19, 6507–6525, 2025
https://doi.org/10.5194/tc-19-6507-2025-supplement
© Author(s) 2025. CC BY 4.0 License.

The Cryosphere Open Access EGU

Supplement of

Multi-model estimate of Antarctic ice-shelf basal mass budget and ocean drivers

Benjamin K. Galton-Fenzi et al.

Correspondence to: Benjamin K. Galton-Fenzi (ben.galton-fenzi@aad.gov.au)

The copyright of individual parts of the supplement might differ from the article licence.

S1 Model setup

Table S1. Further details of the models used in this study. Details for each model can be found in the corresponding primary reference for each model supplied in the main text.

Identifier	Domain	Atmosphere forcing	Sea ice	Ice shelf geometry	Vertical coordinate	Surface resolution	Ice shelf frazil	Ice shelf fluxes
COCO	Global	ERA-Interim[1]	2-layer	RTopo-2[2]	z [4]	5 m	no	uppermost
DINN[a]	Regional	ERA-Interim	Budgell	RTopo-2[3]	s	variable	yes	uppermost
E302	Global	Fully coupled[4]	MPAS-SI	Bedmap2[5]	$z^\star$ [6]	variable[6]	no	distributed[7]
FESH	Global	ERA-Interim	2-layer	RTopo-1.05[8]	z-σ [9]	variable[9]	no	uppermost
FESL	Global	ERA-Interim	2-layer	RTopo-1.05	z-σ [9]	variable[9]	no	uppermost
METR[b]	Regional	ERA-Interim	CICE	RTopo-1.05	s	variable	yes	uppermost
NE01	Global	COSMO-CLM	LIM	Bedmachine[10]	$z^\star$ [1]	variable	no	distributed[11]
NE02	Global	COSMO-CLM	LIM	Bedmachine[12]	$z^\star$ [1]	variable	no	distributed[11]
RICH[c]	Regional	ERA-Interim[13]	Prescribed[13]	Bedmap2/RTopo-2[14]	s	variable	no	uppermost

[1] Dee et al. (2011).

[2] Schaffer et al. (2016).

[3] Including updates for the Amundsen Sea Embayment (Millan et al., 2017).

[4] partial step following Losch (2008).

[4] The 150 years are taken from a coupled atmosphere-ocean-sea-ice-land preindustrial simulation (repeat 1850).

[5] Fretwell et al. (2013).

[6] With adjustments for the top layer to follow the ice draft.

[7] Driving fluxes are the average, and meltwater production is distributed vertically, over the upper 10 m following Gwyther et al. (2020).

[8] Timmermann et al. (2010).

[9] 22 layer σ (equally spaced) coordinate under ice shelves.

[10] Morlighem et al. (2020).

[11] Estimated by calculating the driving fluxes as a mean over the upper 10 m, as with [5] (Mathiot et al., 2017).

[12] Bedmachine data was interpolated to the ice sheet model domain derived from the initialization and relaxation procedure of f.ETISh (Pelletier et al., 2022).

[13] Sea ice fluxes are prescribed, combining atmospheric reanalysis with satellite estimates of sea ice production (Tamura et al., 2011).

[14] Blended product including several local and regional modifications.

[a] DINN forces the lateral temperature and salinity fields to the World Ocean Atlas 2009 (WOA09 Boyer et al., 2009). Depth-averaged velocity and sea surface height are from monthly climatologies derived from the Simple Ocean Data Assimilation (SODA, version 1.4.2) ocean reanalysis (Carton and Giese, 2008).

[b] METR forces the lateral temperature, salinity and velocities using the ECCO2 reanalysis (Menemenlis et al., 2008) and the sea surface height using the AVISO satellite data product (https://www.aviso.altimetry.fr/).

[c] RICH forces the lateral temperature, salinity, velocities and sea surface height using the ECCO2 reanalysis (Menemenlis et al., 2008). A total of 13 major tidal constituents (M2, S2, N2, K2, K1, O1, P1, Q1, MF, MM, M4, MS4, MN4) are derived from the global tidal solution TPXO7.2 (Egbert and Erofeeva, 2002) and also introduced along the northern boundaries using sea surface height and barotropic currents.

S2 Methods

S2.1 Veronni tessellation

Whilst the Voronoi tessellation approach is less commonly applied in geophysical sciences compared to interpolation methods like bilinear or nearest neighbour, it offers several distinct advantages that motivated our selection. Firstly, Voronoi tessellation avoids artificial smoothing by assigning each output cell the value of the nearest input point. This contrasts with bilinear interpolation, which blends surrounding values and may introduce artifacts—especially near boundaries or steep spatial gradients. The method was adaptive to the use of several model outputs which all have different, and irregular meshes and avoids the extrapolation bias inherent in nearest-neighbour and bilinear methods, which can produce misleading values in sparsely sampled or irregularly distributed datasets (See Figure S1). The Voronoi approach inherently adapts to the spatial configuration of the input data, providing a natural partitioning of space that reflects data density. Lastly, it is reproducible and parameter-free. With no tunable parameters this method is deterministic and does not rely on user-defined parameters, ensuring consistency and reduced subjectivity in the data processing. These characteristics made Voronoi tessellation particularly suitable for our use in this case, where spatial heterogeneity and edge preservation were critical in comparing several model outputs. See Okabe et al. (2000) and Shepard (1968) for more information.

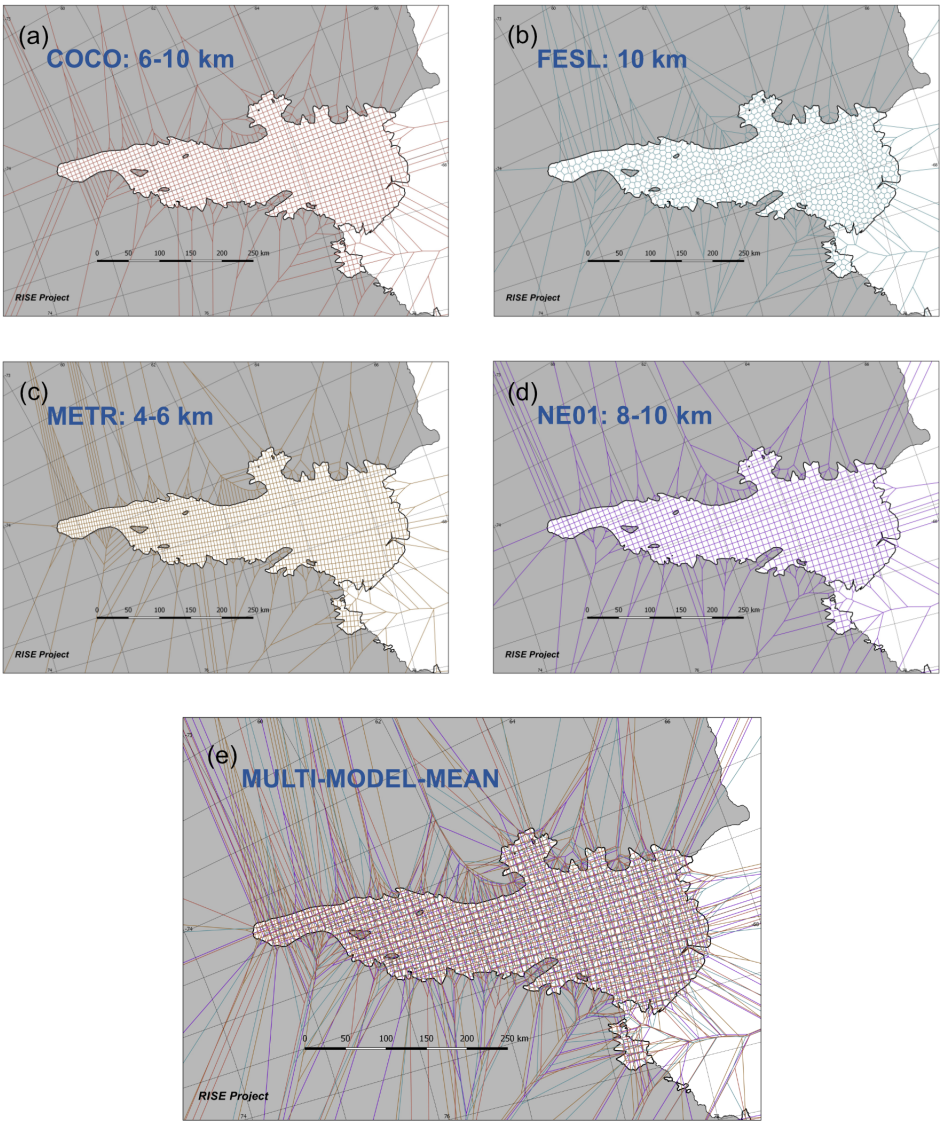

Figure S1. Examples of the Veronni tessellation for the Amery Ice Shelf, used for 4 different models and associated different horizontal resolutions and native mesh type, and how they overlap to produce the Multi-Model Mean for a) COCO, b) FESL, c) METR, d) NE01 and e) MMM.

S3 The Multi-Model Mean (MMM) approach

Each numerical model has a distribution that represents its prediction of basal ice melt. Due to the complexity of the underlying physical processes, individual models inherently possess distinct biases and uncertainties reflected in the spread and shape of their respective distributions. Consequently, some models may overestimate or underestimate the melt rates or their spatial variability. However, when these models are averaged, the central tendency of the ensemble tends to converge toward a more robust estimate of the true state. This behaviour is consistent with statistical theory, particularly the 'central limit theorem', where the average of multiple independent estimators tends toward a Gaussian distribution, even if individual models are not normally distributed. The ensemble mean thus serves to reduce individual biases and smooth out uncertainties, resulting in a more reliable representation of basal melt. This "Gaussian phenomenon" of multi-model averaging is well documented in the climate modelling literature. For example: Tebaldi and Knutti (2007) highlight the statistical benefits of ensemble averaging for climate projections, particularly in reducing bias and quantifying uncertainty; Gleckler et al. (2008) show that multi-model means often outperform individual models based on performance metrics; Smith et al. (2009) provide a Bayesian framework that supports the Gaussian nature of multi-model means and their improved predictive accuracy; Knutti and Sedláček (2013) emphasise how multi-model means enhance robustness and reliability in CMIP5 projections. The MMM represents a useful benchmark for assessing model diversity and guiding observational design and model development.

S4 Comparison with satellite observations

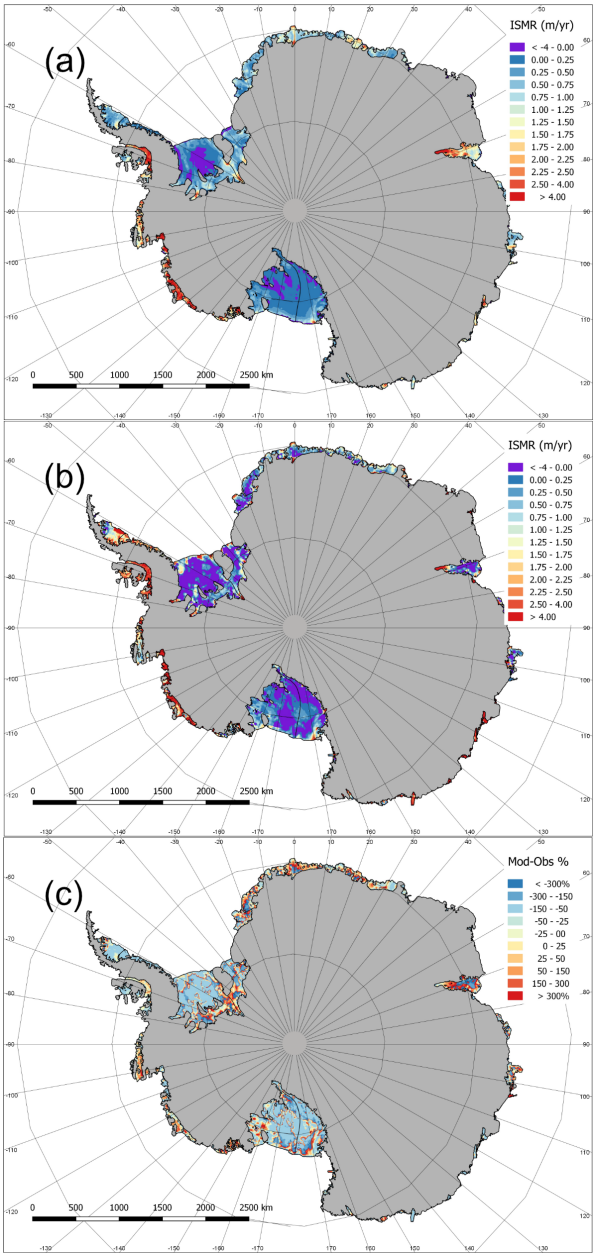

Figure S2. Comparison of melt rates between a) the Multi-model Mean (MMM) and b) Satellite based estimates (SATT). c) is the percentage difference between MMM and SATT, calculated as (MMM - SATT)/ SATT)$\times 100$

S5 Individual Ice Shelf examples

S5.1 Amery Ice Shelf

Table S2. Amery Ice Shelf, East Antarctica

Identifier	Cavity Volume (km^3)	Melt rate (m $year^{-1}$)	Mass loss (Gt $year^{-1}$) Net	Melt	Freeze	Freeze/Melt $\times 100$ (%)
MMM	31823	1.54	85.59	86.24	0.64	0.74
COCO	29682	0.78	43.59	45.26	1.67	3.69
DINN	27981	0.40	22.34	24.95	2.61	10.46
E302	34595	4.16	231.88	231.88	0.00	0.00
FESH	38125	1.17	65.38	71.45	6.07	8.50
FESL	38959	1.23	68.67	73.84	5.17	7.00
METR	32806	1.43	79.60	80.48	0.88	1.09
NE01	30631	3.00	167.41	167.47	0.06	0.04
NE02	29990	1.45	80.71	80.72	0.01	0.01
RICH	23634	0.19	10.77	16.90	6.13	36.27
SATT	-	0.90	49.59	61.17	11.58	18.93

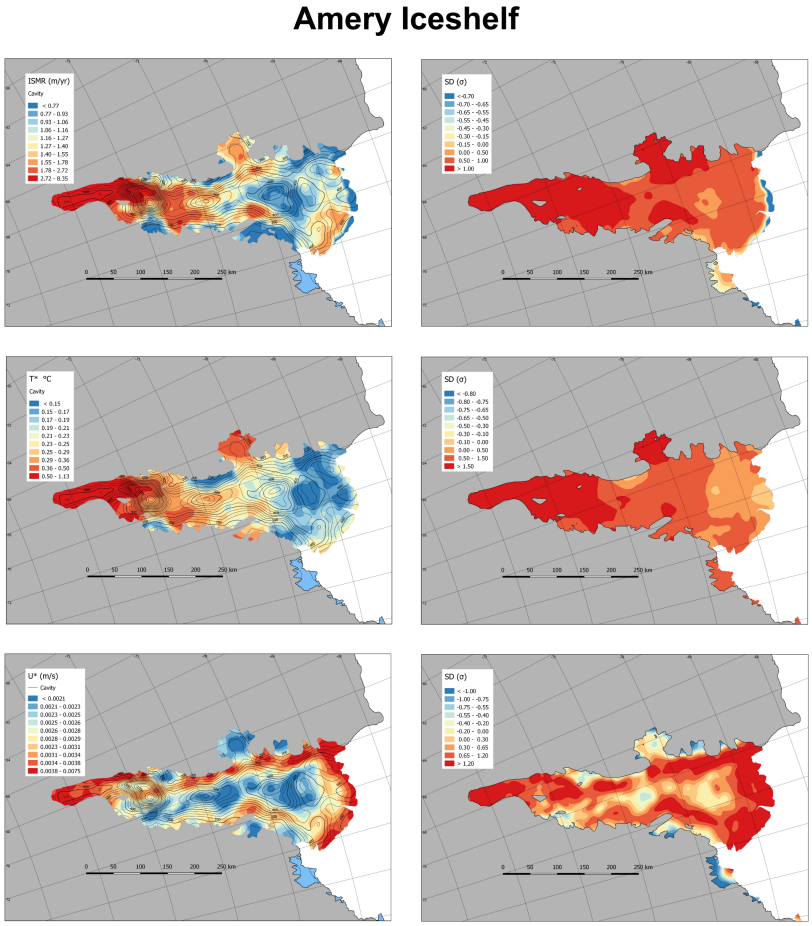

Figure S3. Maps of the Amery Ice Shelf, East Antarctica, for the Multi-Model Mean, of the ice shelf melt rate (ISMR, top-left), $T^\star$ (middle-left), $u^\star$ (bottom-left) and their corresponding standard deviation across the models (right-hand panels).

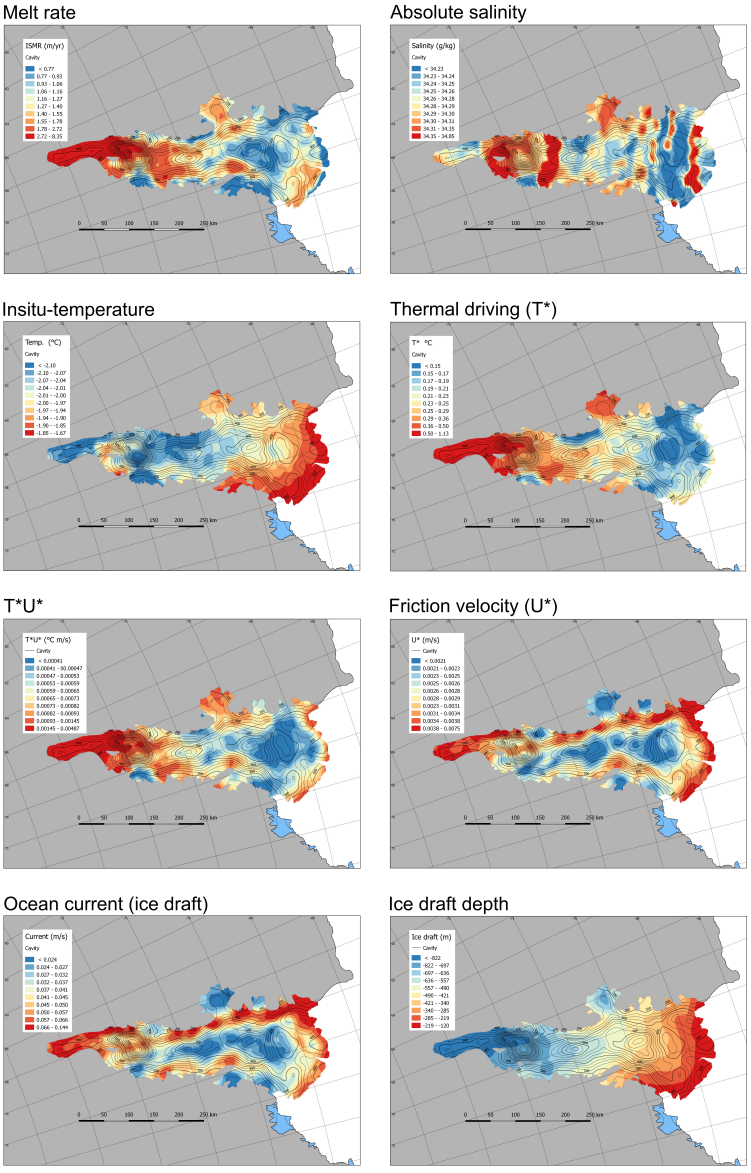

Figure S4. Maps of the Amery Ice Shelf, East Antarctica, for the Multi-Model Mean.

S5.2 Fimbul Ice Shelf

Table S3. Fimbul Ice Shelf, East Antarctica

Identifier	Cavity Volume (km^3)	Melt rate (m $year^{-1}$)	Mass loss (Gt $year^{-1}$) Net	Melt	Freeze	Freeze/Melt $\times 100$ (%)
MMM	46698	0.94	35.43	35.55	0.12	0.34
COCO	48129	1.93	72.38	72.38	0.00	0.00
DINN	48290	1.18	44.16	44.60	0.44	0.99
E302	49838	0.83	31.34	31.34	0.00	0.00
FESH	46832	0.99	37.09	43.19	6.10	14.12
FESL	48742	0.84	31.47	35.45	3.97	11.20
METR	39290	0.55	20.56	20.57	0.01	0.05
NE01	45447	0.40	14.87	14.88	0.01	0.07
NE02	45806	0.34	12.88	12.88	0.00	0.00
RICH	47907	1.44	54.12	54.18	0.06	0.11
SATT	-	0.88	32.81	35.64	2.82	7.91

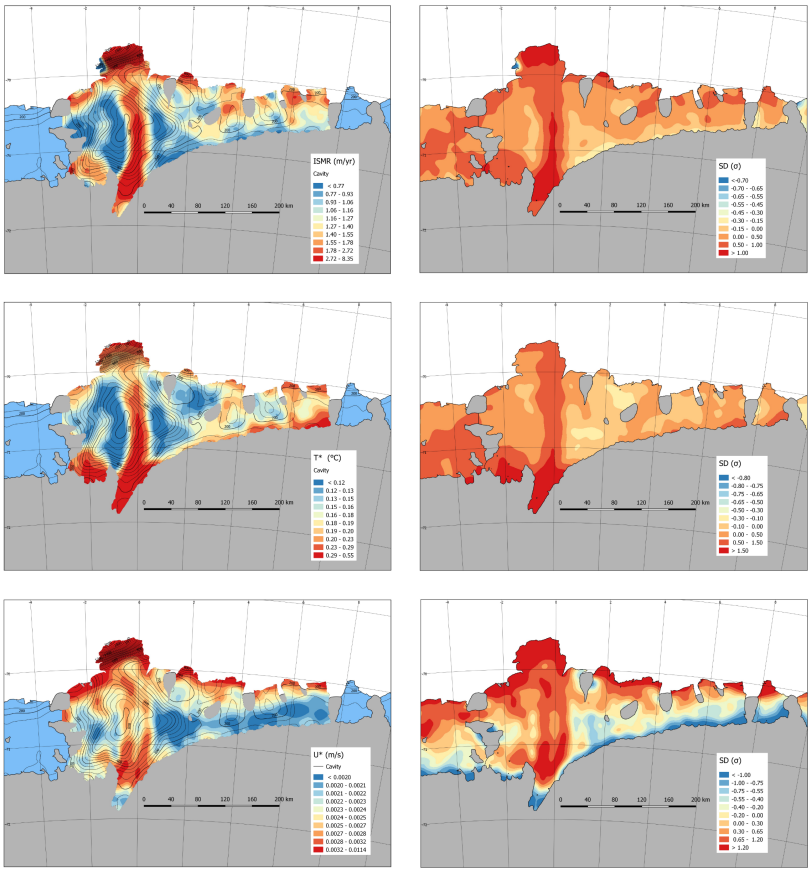

Figure S5. Maps of the Fimbul Ice Shelf, East Antarctica, for the Multi-Model Mean, of the ice shelf melt rate (ISMR, top-left), $T^\star$ (middle-left), $u^\star$ (bottom-left) and their corresponding standard deviation across the models (right-hand panels).

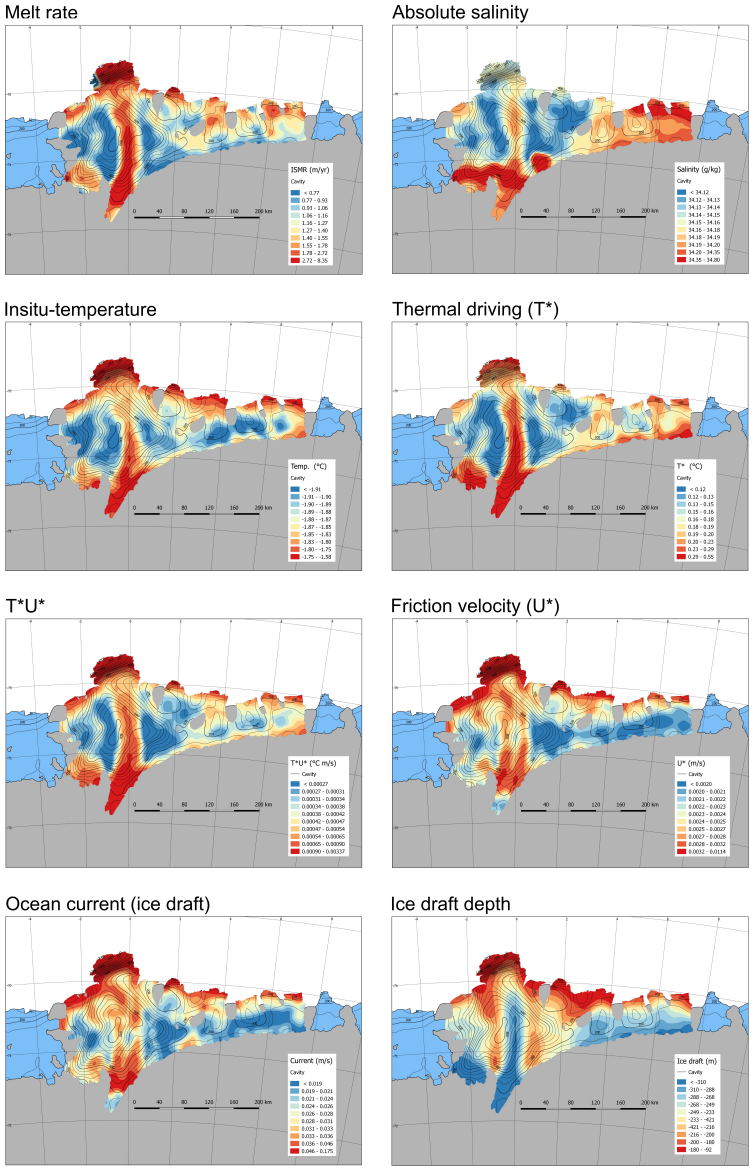

Figure S6. Maps of the Fimbul Ice Shelf, East Antarctica, for the Multi-Model Mean.

S5.3 Larsen Ice Shelf

Table S4. Larsen C, Antarctic Peninsula

Identifier	Cavity Volume (km^3)	Melt rate (m $year^{-1}$)	Mass loss (Gt $year^{-1}$) Net	Melt	Freeze	Freeze/Melt $\times 100$ (%)
MMM	21512	0.59	25.56	25.59	0.03	0.12
COCO	22027	0.54	23.54	23.59	0.05	0.21
DINN	20996	0.34	14.71	15.04	0.33	2.19
E302	22624	0.65	28.35	28.35	0.00	0.00
FESH	23407	1.23	53.47	55.11	1.63	2.96
FESL	24716	0.83	36.14	38.86	2.72	7.00
METR	21585	0.39	16.97	16.97	0.00	0.00
NE01	19577	0.60	26.00	26.03	0.02	0.08
NE02	20497	0.49	21.50	21.51	0.01	0.05
RICH	18183	0.22	9.37	10.48	1.10	10.50
SATT	-	1.67	65.31	66.19	0.87	1.31

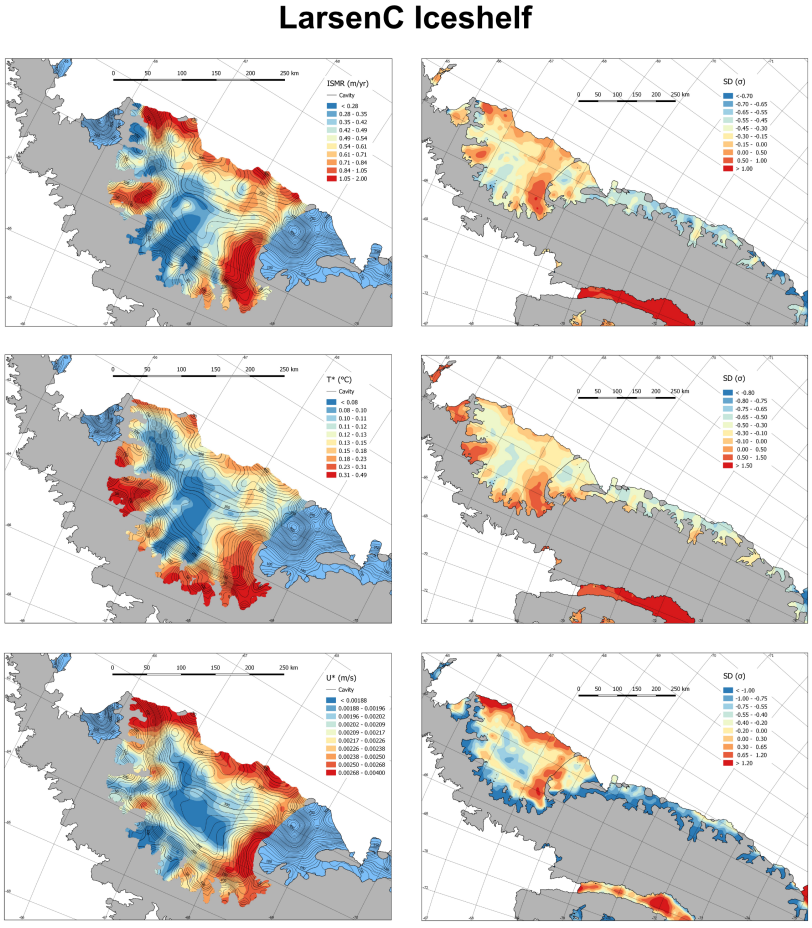

Figure S7. Maps of the Larsen C Ice Shelf, Antarctic Peninsula, for the Multi-Model Mean, of the ice shelf melt rate (ISMR, top-left), $T^\star$ (middle-left), $u^\star$ (bottom-left) and their corresponding standard deviation across the models (right-hand panels).

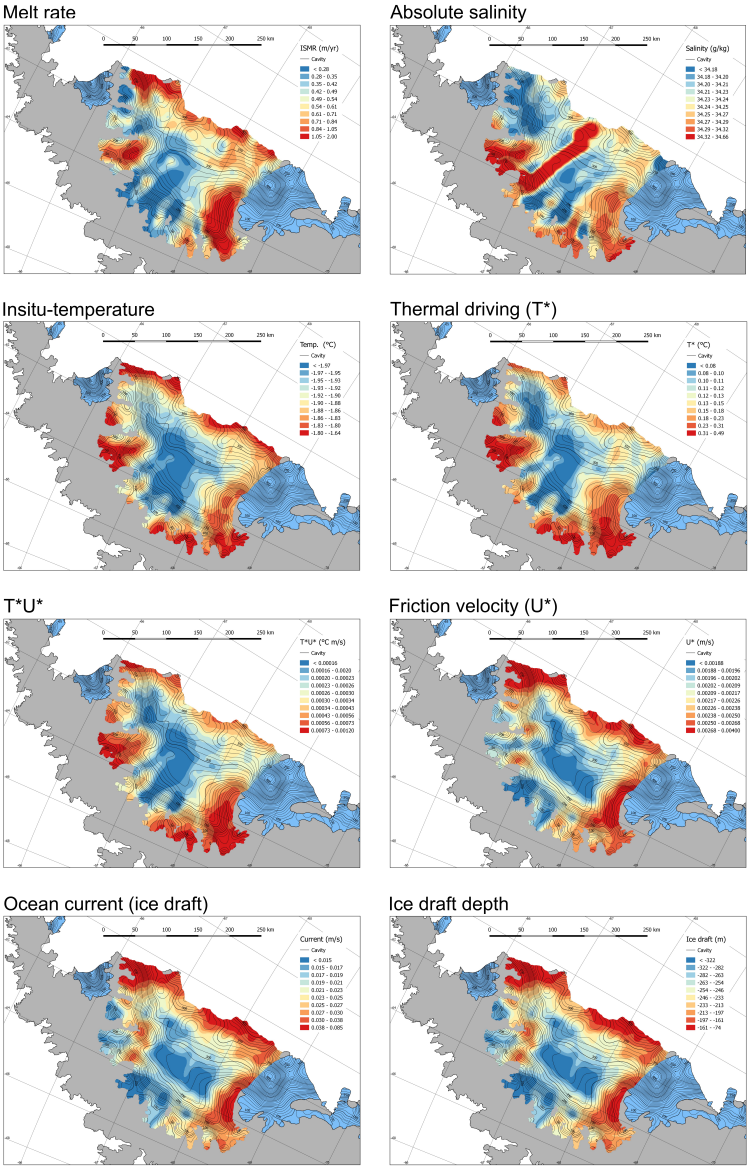

Figure S8. Maps of the Larsen C Ice Shelf, Antarctic Peninsula, for the Multi-Model Mean.

S5.4 Ronne-Filchner Ice Shelf, East Antarctica

Table S5. Ronne-Filchner Ice Shelf, East Antarctica

Identifier	Cavity Volume (km^3)	Melt rate (m $year^{-1}$)	Mass loss (Gt $year^{-1}$)			Freeze/Melt $\times 100$ (%)
			Net	Melt	Freeze	
MMM	148092	0.21	62.95	75.26	12.31	16.36
COCO	160448	0.23	69.39	94.42	25.03	26.51
DINN	153642	0.09	25.76	64.00	38.24	59.75
E302	167984	0.30	91.18	93.37	2.18	2.33
FESH	152412	0.17	50.02	58.20	8.18	14.05
FESL	160461	0.16	47.29	55.55	8.26	14.87
METR	143434	0.10	29.38	39.91	10.53	26.38
NE01	133179	0.32	97.35	126.98	29.63	23.33
NE02	131269	0.24	73.08	94.95	21.87	23.03
RICH	130002	0.28	83.11	103.98	20.88	20.08
SATT	-	0.07	21.76	120.83	99.06	81.98

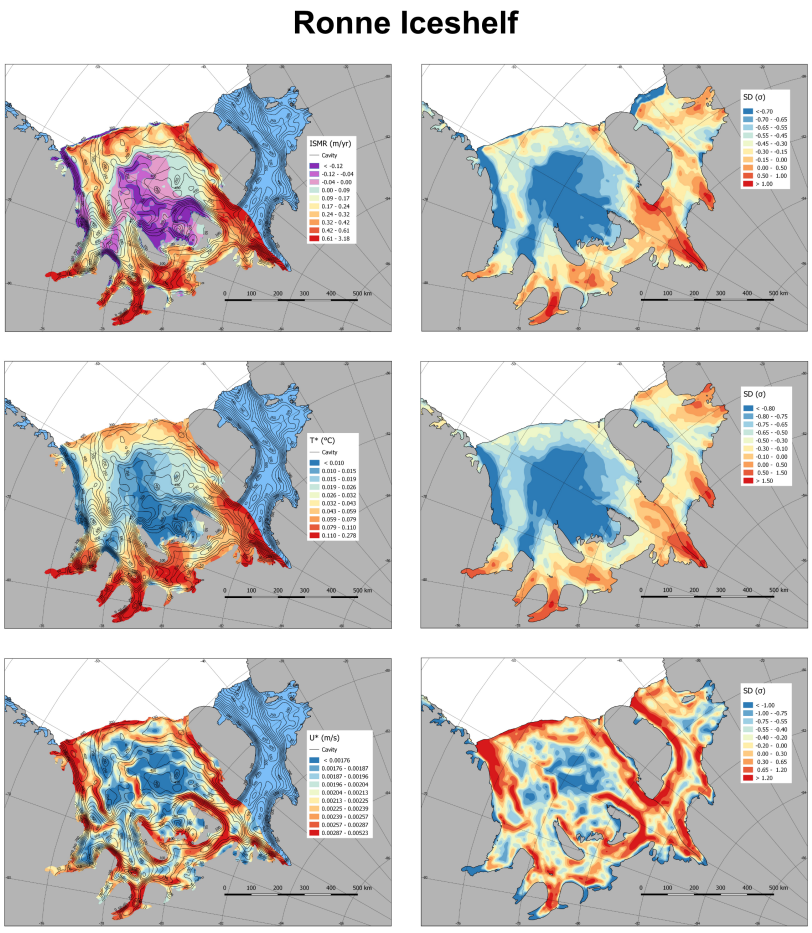

Figure S9. Maps of the Ronne-Filchner Ice Shelf, East Antarctica, for the Multi-Model Mean, of the ice shelf melt rate (ISMR, top-left), $T^\star$ (middle-left), $u^\star$ (bottom-left) and their corresponding standard deviation across the models (right-hand panels).

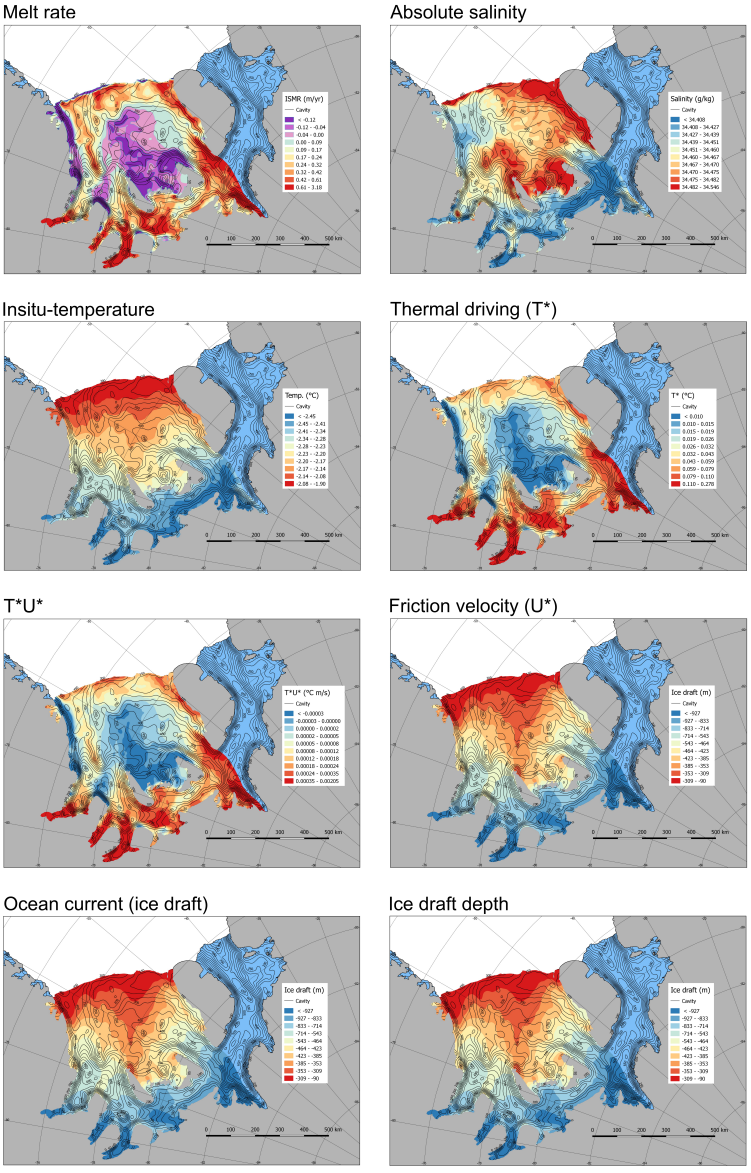

Figure S10. Maps of the Ronne-Filchner Ice Shelf, East Antarctica, for the Multi-Model Mean.

S5.5 Ross Ice Shelf, West Antarctica

Table S6. Ross Ice Shelf, West Antarctica

Identifier	Cavity Volume (km^3)	Melt rate (m $year^{-1}$)	Mass loss (Gt $year^{-1}$)			Freeze/Melt $\times 100$ (%)
			Net	Melt	Freeze	
MMM	234993	0.16	78.23	68.31	9.94	14.55
COCO	245992	0.26	122.97	113.94	9.03	7.93
DINN	235836	0.11	70.94	49.42	21.52	43.55
E302	236100	0.15	69.05	67.60	1.45	2.14
FESH	244455	0.16	117.82	69.18	48.63	70.29
FESL	253107	0.15	100.72	67.07	33.65	50.17
METR	237892	0.13	60.03	57.72	2.31	4.00
NE01	218505	0.15	74.02	67.46	6.56	9.72
NE02	217227	0.13	59.95	57.98	1.97	3.40
RICH	225819	0.15	71.35	64.33	7.01	10.90
SATT	-	0.13	113.93	58.24	55.69	95.62

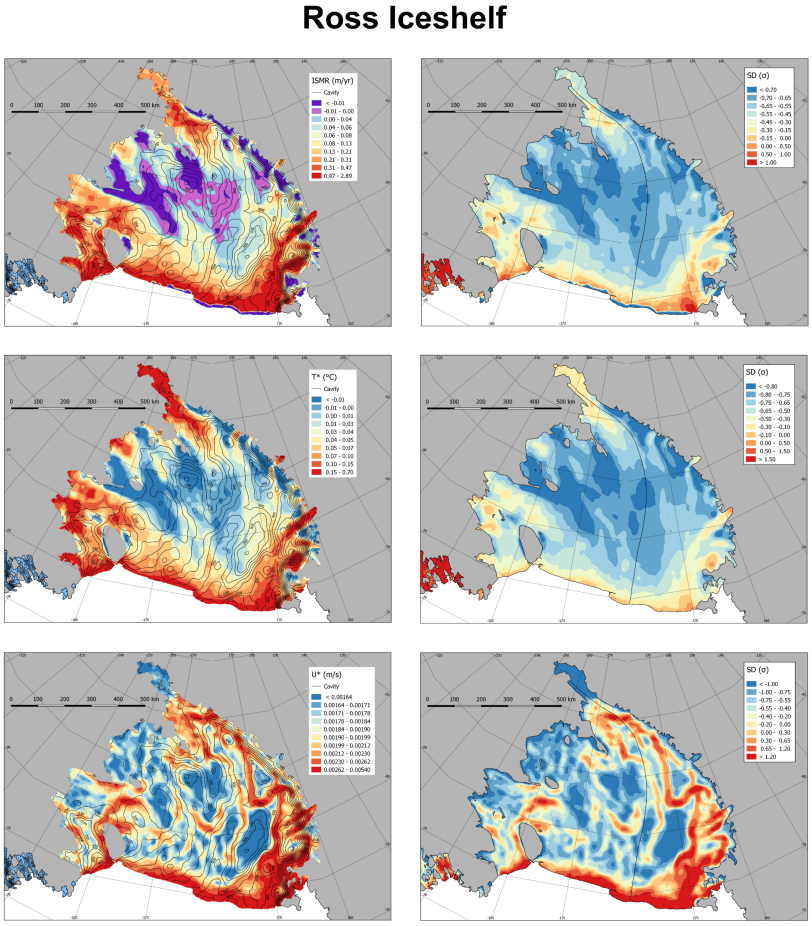

Figure S11. Maps of the Ross Ice Shelf, West Antarctica, for the Multi-Model Mean, of the ice shelf melt rate (ISMR, top-left), $T^\star$ (middle-left), $u^\star$ (bottom-left) and their corresponding standard deviation across the models (right-hand panels).

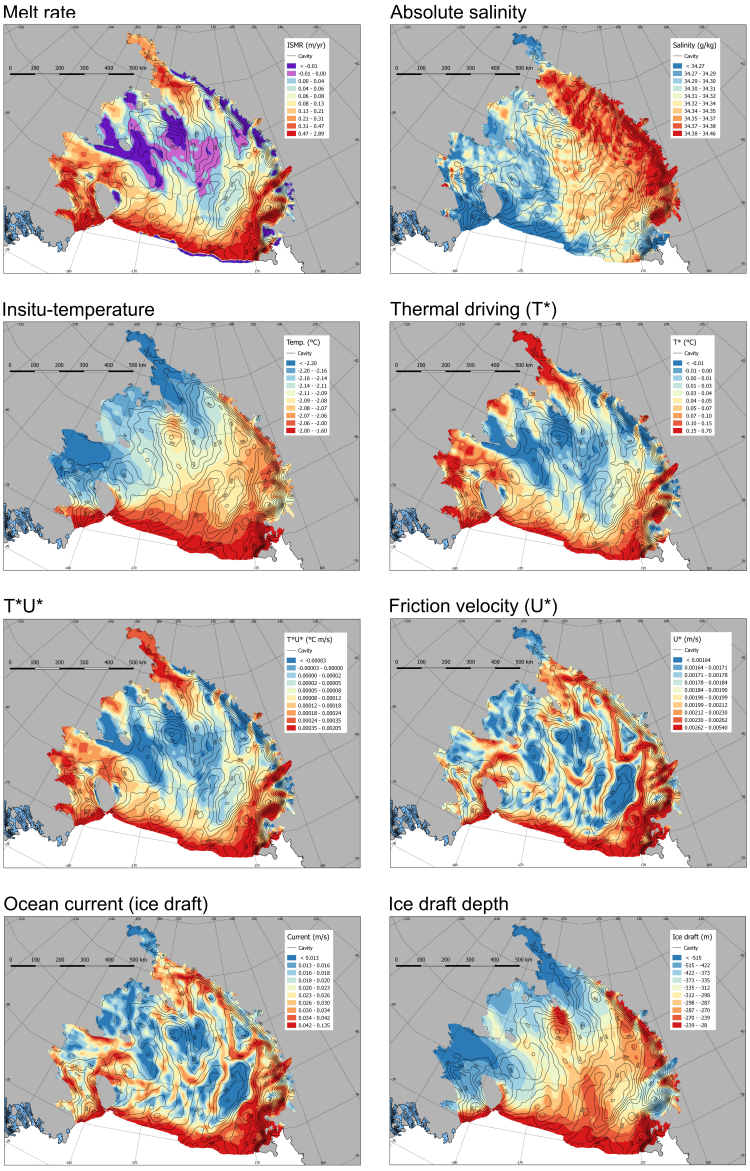

Figure S12. Maps of the Ross Ice Shelf, West Antarctica, for the Multi-Model Mean.

S5.6 Thwaites Ice Shelf, West Antarctica

Table S7. Thwaites Ice Shelf, West Antarctica

Identifier	Cavity Volume (km^3)	Melt rate (m $year^{-1}$)	Mass loss (Gt $year^{-1}$) Net	Melt	Freeze	Freeze/Melt $\times 100$ (%)
MMM	4845	3.04	14.99	15.53	0.54	3.48
COCO	4762	1.42	6.99	6.99	0.00	0.00
DINN	4352	4.57	22.54	23.29	0.75	3.22
E302	5226	1.17	5.78	5.78	0.00	0.00
FESH	5353	0.30	1.48	6.60	5.12	77.58
FESL	5732	0.10	0.51	3.57	3.07	85.99
METR	4537	1.58	7.81	7.81	0.00	0.00
NE01	4925	3.77	18.56	18.56	0.00	0.00
NE02	5099	8.17	40.28	40.28	0.00	0.00
RICH	3623	6.28	30.96	30.97	0.02	0.06
SATT	-	29.71	81.04	81.05	0.00	0.00

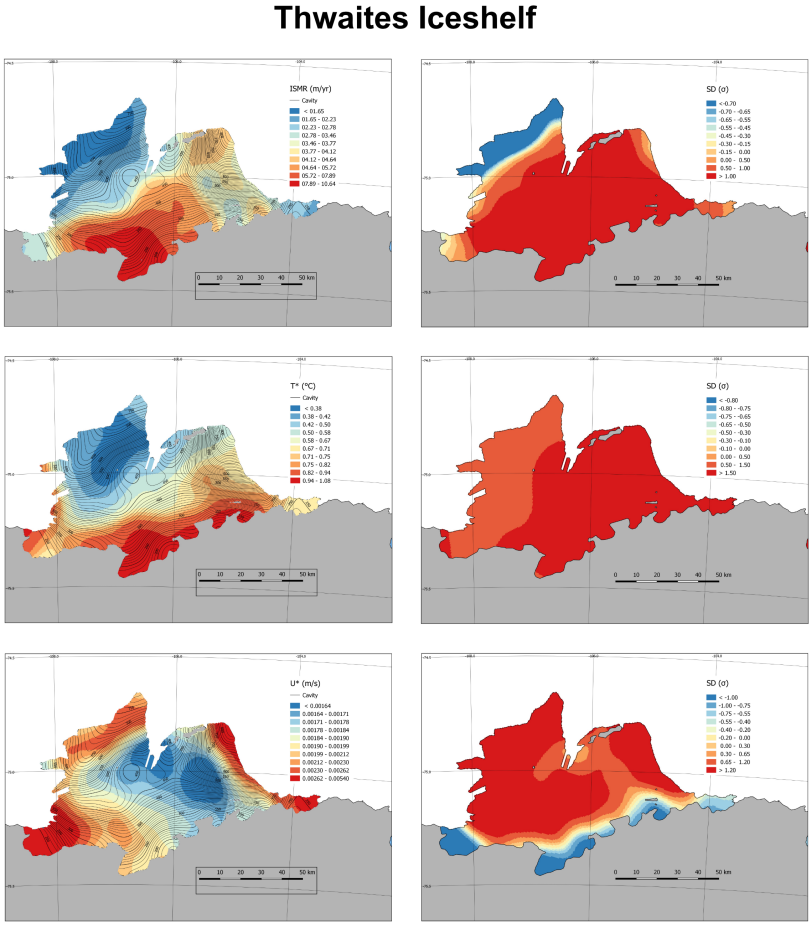

Figure S13. Maps of the Thwaites Ice Shelf, West Antarctica, for the Multi-Model Mean, of the ice shelf melt rate (ISMR, top-left), $T^\star$ (middle-left), $u^\star$ (bottom-left) and their corresponding standard deviation across the models (right-hand panels).

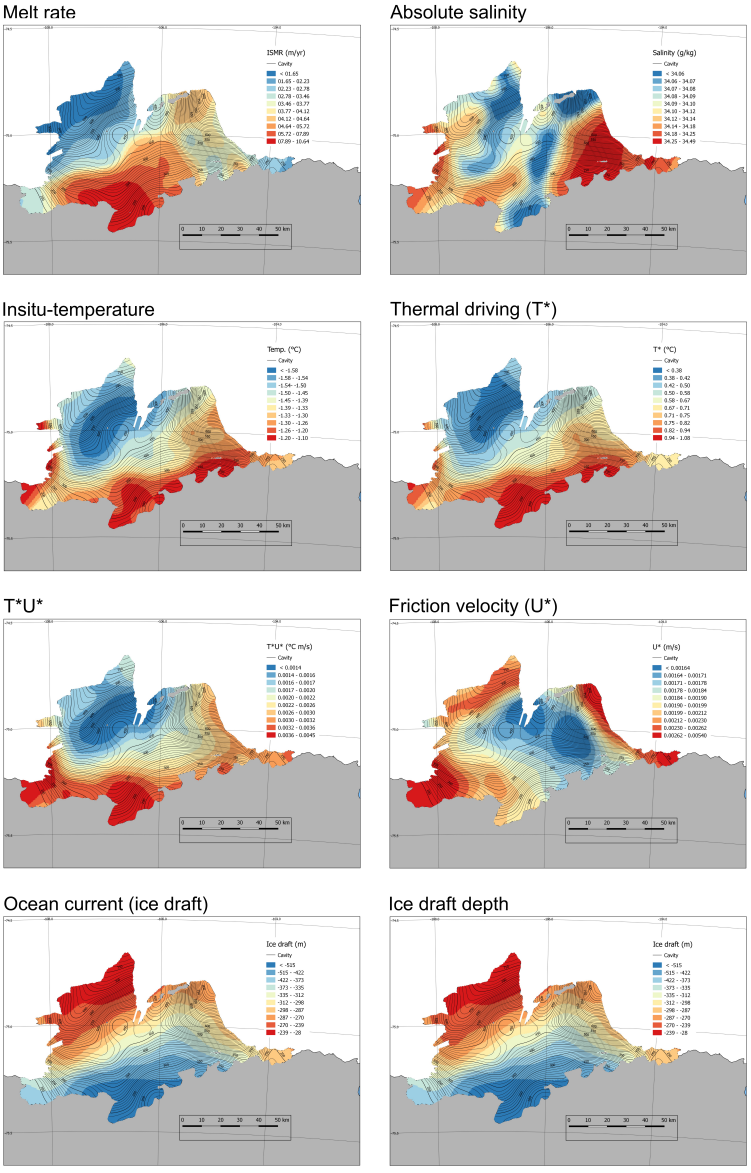

Figure S14. Maps of the Thwaites Ice Shelf, West Antarctica, for the Multi-Model Mean.

S5.7 Totten Ice Shelf, East Antarctica.

Table S8. Totten Ice Shelf, East Antarctica

Identifier	Cavity Volume (km^3)	Melt rate (m $year^{-1}$)	Mass loss (Gt $year^{-1}$) Net	Melt	Freeze	Freeze/Melt $\times 100$ (%)
MMM	2482	2.23	12.63	12.64	0.01	0.08
COCO	2282	1.50	8.52	8.52	0.00	0.00
DINN	1367	0.43	2.45	2.54	0.10	3.94
E302	4316	2.69	15.27	15.27	0.00	0.00
FESH	2433	1.31	7.43	7.73	0.30	3.88
FESL	3044	0.79	4.50	4.59	0.10	2.18
METR	1076	0.71	4.05	4.05	0.00	0.00
NE01	3886	5.37	30.46	30.46	0.00	0.00
NE02	3439	6.00	34.04	34.04	0.00	0.00
RICH	499	1.23	6.98	8.06	1.07	13.28
SATT	-	10.65	59.39	60.04	0.65	-1.08

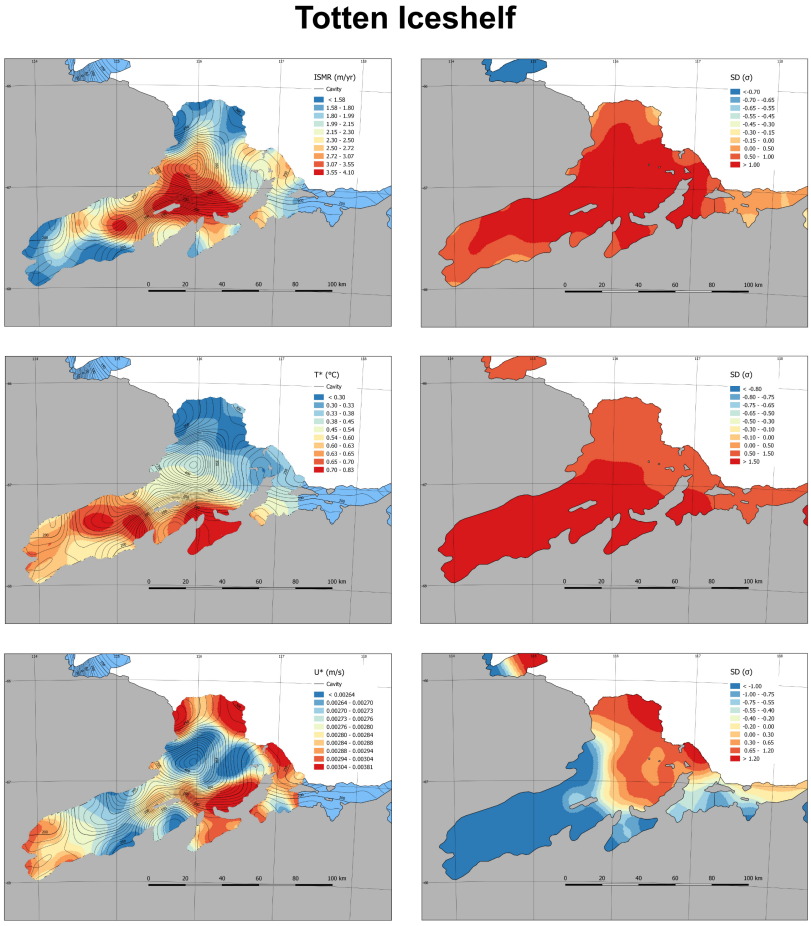

Figure S15. Maps of the Totten Ice Shelf, East Antarctica, for the Multi-Model Mean, of the ice shelf melt rate (ISMR, top-left), $T^\star$ (middle-left), $u^\star$ (bottom-left) and their corresponding standard deviation across the models (right-hand panels).

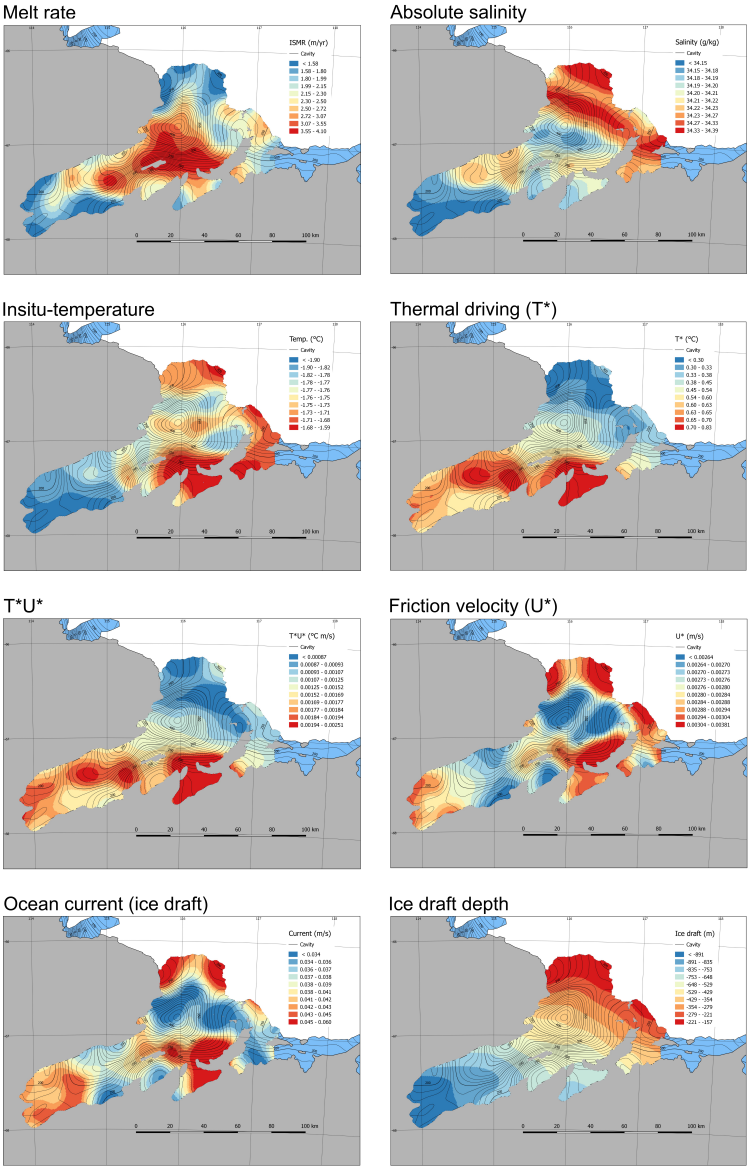

Figure S16. Maps of the Totten Ice Shelf, East Antarctica, for the Multi-Model Mean.

S6 Comparison of contributing model results for Antarctica

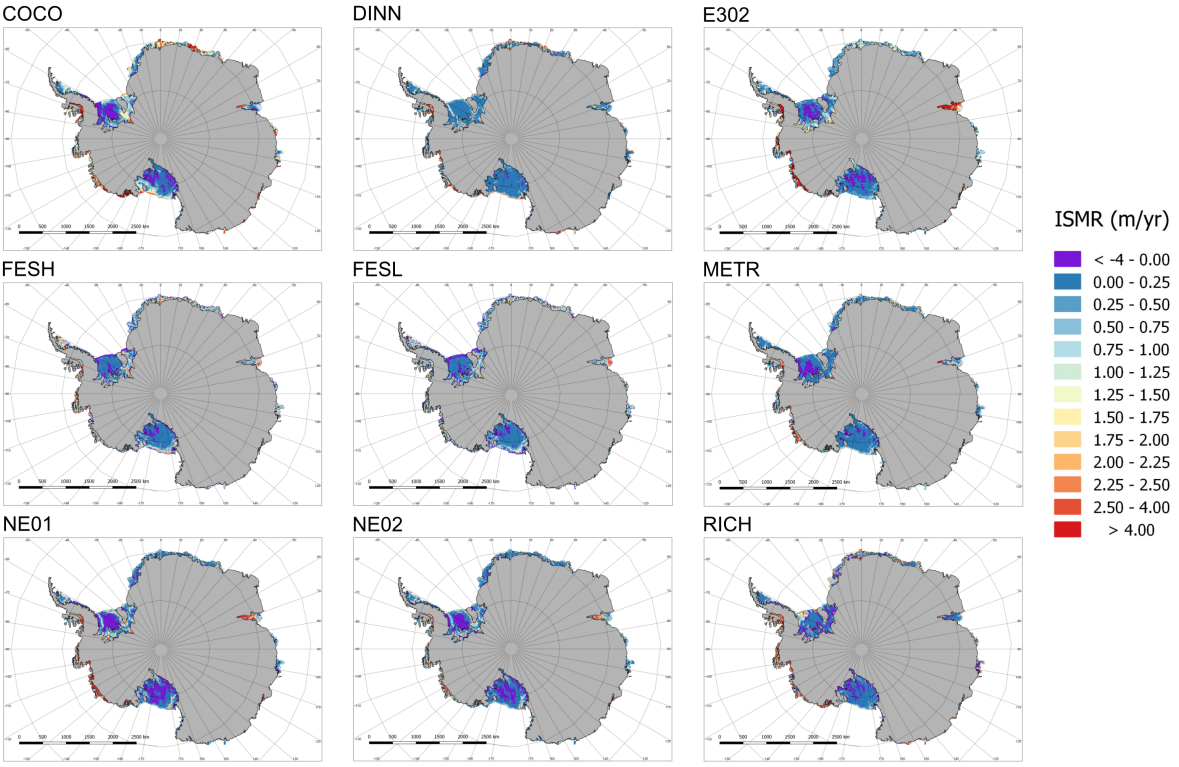

Figure S17. Melt rates, m (m year^{-1}), across all models.

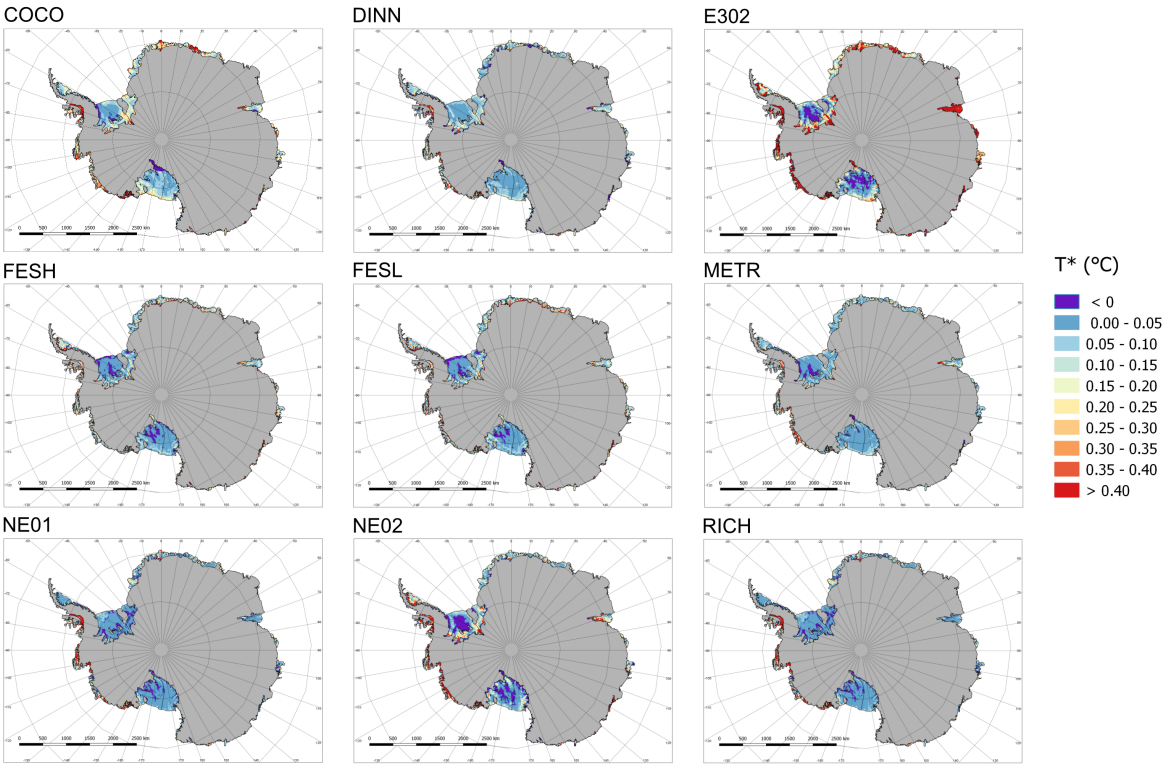

Figure S18. Thermal driving, $T^{\star}$ ($^{\circ}C$), across all models.

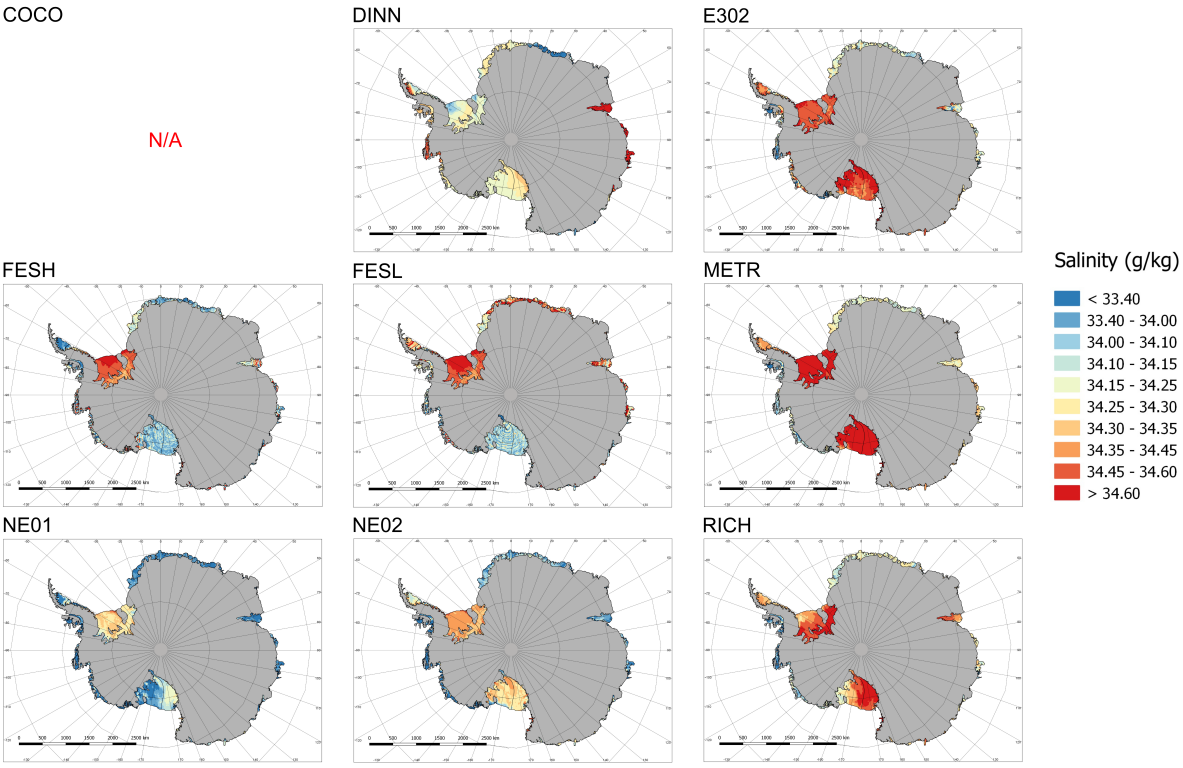

Figure S19. Absolute Salinity at the base of the ice shelf, S_A (g kg^{-1}), across all models.

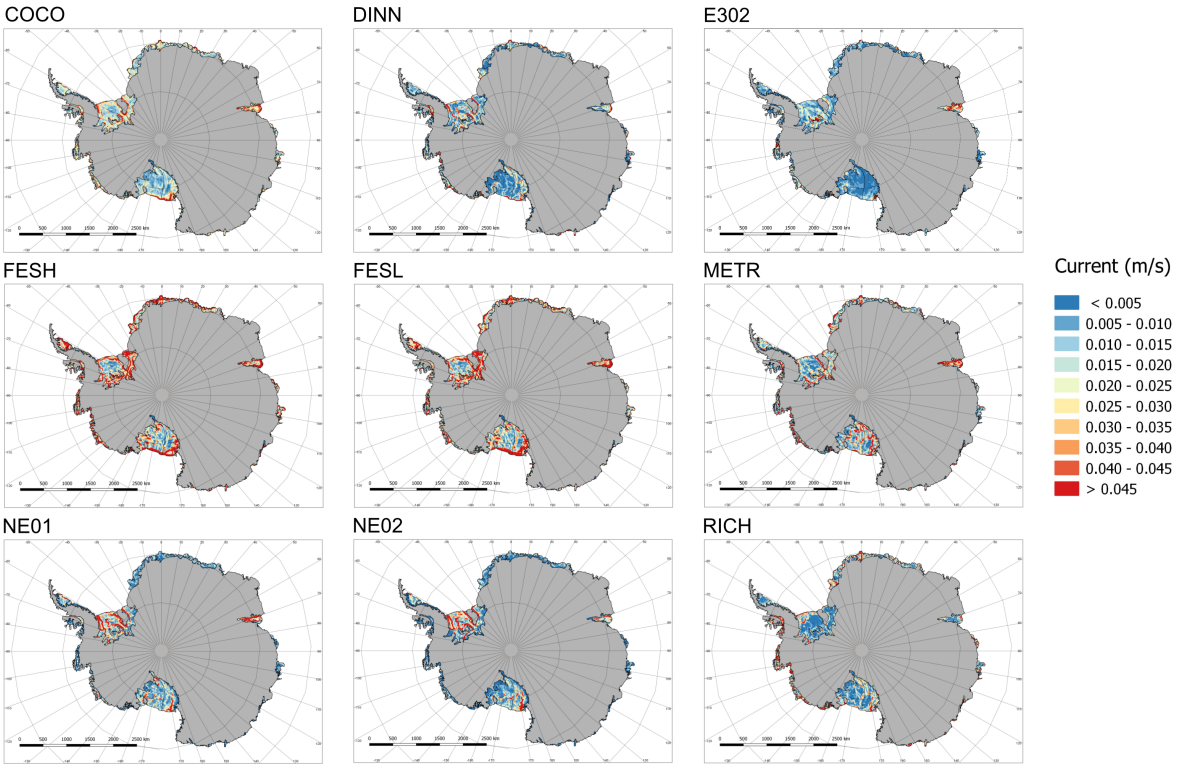

Figure S20. Ocean current speed at the ice shelf base, u_m (m s^{-1}), across all models.

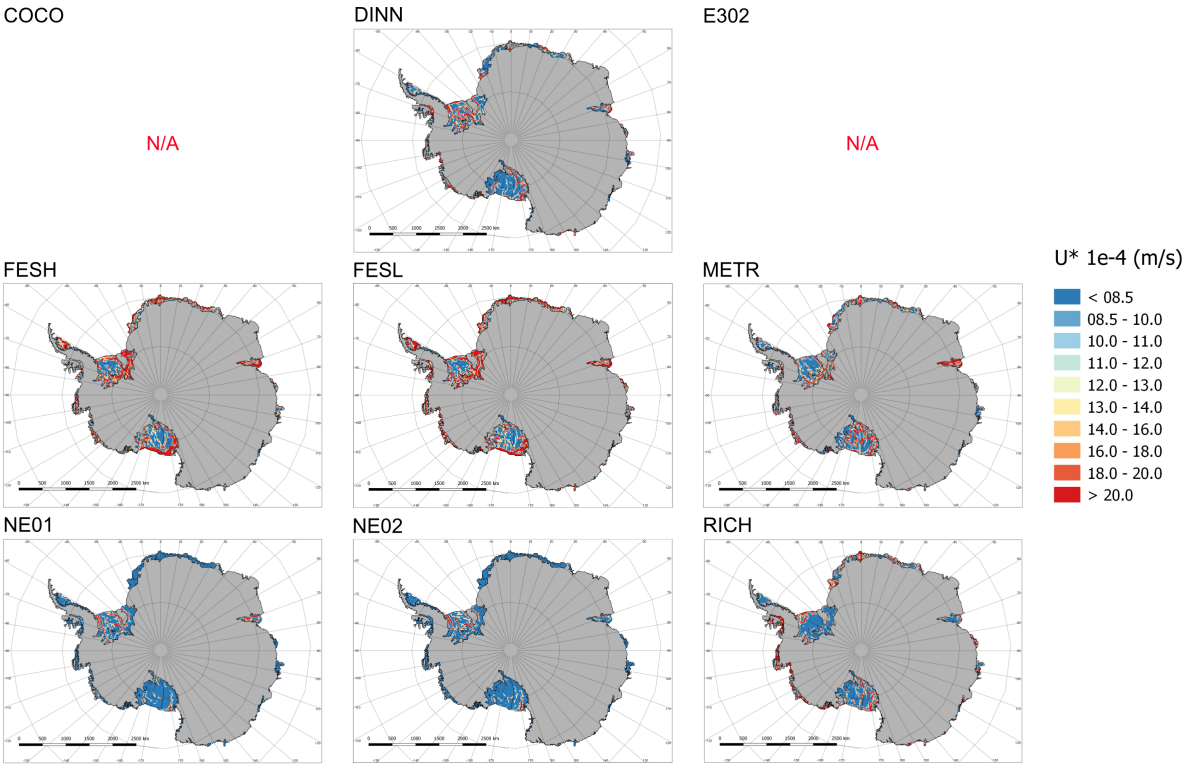

Figure S21. Friction velocity, $u^{\star}$ (m s^{-1}), across all models.

References

Boyer, T. P., Antonov, J. I., Baranova, O. K., Garcia, H. E., Johnson, D. R., Mishonov, A. V., O'Brien, T. D., Seidov, D., Smolyar, I., Zweng, M. M., et al.: World ocean database 2009, 2009.

Carton, J. A. and Giese, B. S.: A reanalysis of ocean climate using Simple Ocean Data Assimilation (SODA), Monthly weather review, 136, 2999–3017, 2008.

Dee, D. P., Uppala, S. M., Simmons, A. J., Berrisford, P., Poli, P., Kobayashi, S., Andrae, U., Balmaseda, M., Balsamo, G., Bauer, d. P., et al.: The ERA-Interim reanalysis: Configuration and performance of the data assimilation system, Quarterly Journal of the royal meteorological society, 137, 553–597, 2011.

Egbert, G. D. and Erofeeva, S. Y.: Efficient inverse modeling of barotropic ocean tides, Journal of Atmospheric and Oceanic technology, 19, 183–204, 2002.

Fretwell, P., Pritchard, H. D., Vaughan, D. G., Bamber, J. L., Barrand, N. E., Bell, R., Bianchi, C., Bingham, R., Blankenship, D. D., Casassa, G., et al.: Bedmap2: improved ice bed, surface and thickness datasets for Antarctica, The cryosphere, 7, 375–393, 2013.

Gleckler, P. J., Taylor, K. E., and Doutriaux, C.: Performance metrics for climate models, Journal of Geophysical Research: Atmospheres, 113, https://doi.org/https://doi.org/10.1029/2007JD008972, 2008.

Gwyther, D. E., Kusahara, K., Asay-Davis, X. S., Dinniman, M. S., and Galton-Fenzi, B. K.: Vertical processes and resolution impact ice shelf basal melting: A multi-model study, Ocean Modelling, 147, 101 569, 2020.

Knutti, R. and Sedláček, J.: Robustness and uncertainties in the new CMIP5 climate model projections, Nature climate change, 3, 369–373, https://doi.org/https://doi.org/10.1038/NCLIMATE1716, 2013.

Losch, M.: Modeling ice shelf cavities in az coordinate ocean general circulation model, Journal of Geophysical Research: Oceans, 113, 2008.

Mathiot, P., Jenkins, A., Harris, C., and Madec, G.: Explicit representation and parametrised impacts of under ice shelf seas in the z^* coordinate ocean model NEMO 3.6, Geoscientific Model Development, 10, 2849–2874, https://doi.org/10.5194/gmd-10-2849-2017, 2017.

Menemenlis, D., Campin, J.-M., Heimbach, P., Hill, C., Lee, T., Nguyen, A., Schodlok, M., and Zhang, H.: ECCO2: High resolution global ocean and sea ice data synthesis, Mercator Ocean Quarterly Newsletter, 31, 13–21, 2008.

Millan, R., Rignot, E., Bernier, V., Morlighem, M., and Dutrieux, P.: Bathymetry of the Amundsen Sea Embayment sector of West Antarctica from Operation IceBridge gravity and other data, Geophysical Research Letters, 44, 1360–1368, 2017.

Morlighem, M., Rignot, E., Binder, T., Blankenship, D., Drews, R., Eagles, G., Eisen, O., Ferraccioli, F., Forsberg, R., Fretwell, P., et al.: Deep glacial troughs and stabilizing ridges unveiled beneath the margins of the Antarctic ice sheet, Nature geoscience, 13, 132–137, 2020.

Okabe, A., Boots, B., Sugihara, K., and Chiu, S. N.: Spatial Tessellations: Concepts and Applications of Voronoi Diagrams, Wiley, 2 edn., 2000.

Pelletier, C., Fichefet, T., Goosse, H., Haubner, K., Helsen, S., Huot, P.-V., Kittel, C., Klein, F., Le clec'h, S., van Lipzig, N. P. M., Marchi, S., Massonnet, F., Mathiot, P., Moravveji, E., Moreno-Chamarro, E., Ortega, P., Pattyn, F., Souverijns, N., Van Achter, G., Vanden Broucke, S., Vanhulle, A., Verfaillie, D., and Zipf, L.: PARASO, a circum-Antarctic fully coupled ice-sheet–ocean–sea-ice–atmosphere–land model involving f.ETISh1.7, NEMO3.6, LIM3.6, COSMO5.0 and CLM4.5, Geoscientific Model Development, 15, 553–594, https://doi.org/10.5194/gmd-15-553-2022, 2022.

Schaffer, J., Timmermann, R., Arndt, J. E., Kristensen, S. S., Mayer, C., Morlighem, M., and Steinhage, D.: A global, high-resolution data set of ice sheet topography, cavity geometry, and ocean bathymetry, Earth System Science Data, 8, 543–557, https://doi.org/10.5194/essd-8-543-2016, 2016.

Shepard, D.: A two-dimensional interpolation function for irregularly-spaced data, in: Proceedings of the 1968 23rd ACM National Conference, pp. 517–524, https://doi.org/10.1145/800186.810616, 1968.

Smith, R. L., Tebaldi, C., Nychka, D., and Mearns, L. O.: Bayesian modeling of uncertainty in ensembles of climate models, Journal of the American Statistical Association, 104, 97–116, https://doi.org/https://doi.org/10.1198/jasa.2009.0007, 2009.

Tamura, T., Ohshima, K. I., Nihashi, S., and Hasumi, H.: Estimation of Surface Heat/Salt Fluxes Associated with Sea Ice Growth/Melt in the Southern Ocean, SOLA, 7, 17–20, https://doi.org/10.2151/sola.2011-005, 2011.

Tebaldi, C. and Knutti, R.: The use of the multi-model ensemble in probabilistic climate projections, Philosophical Transactions of the Royal Society A: Mathematical, Physical and Engineering Sciences, 365, 2053–2075, https://doi.org/https://doi.org/10.1098/rsta.2007.2076, 2007.

Timmermann, R., Le Brocq, A., Deen, T., Domack, E., Dutrieux, P., Galton-Fenzi, B., Hellmer, H., Humbert, A., Jansen, D., Jenkins, A., Lambrecht, A., Makinson, K., Niederjasper, F., Nitsche, F., Nøst, O. A., Smedsrud, L. H., and Smith, W. H. F.: A consistent data set of Antarctic ice sheet topography, cavity geometry, and global bathymetry, Earth System Science Data, 2, 261–273, https://doi.org/10.5194/essd-2-261-2010, 2010.